RSC Advances

PAPER

View Article Online
View Journal | View Issue

Cite this: *RSC Adv.*, 2022, **12**, 1384

Boosting the catalytic behavior and stability of a gold catalyst with structure regulated by ceria†

Jingjie Luo, ‡ Fengxiang Shan,‡ Sihan Yang, Yixue Zhou and Changhai Liang *

In this work, a series of colloidal gold nanoparticles with controllable sizes were anchored on carbon nanotubes (CNT) for the aerobic oxidation of benzyl alcohol. The intrinsic influence of Au particles on the catalytic behavior was unraveled based on different nanoscale-gold systems. The Au/CNT-A sample with smaller Au sizes deserved a faster reaction rate, mainly resulting from the higher dispersion degree (23.5%) of Au with the available exposed sites contributed by small gold particles. However, monometallic Au/CNT samples lacked long-term stability. CeO_2 was herein decorated to regulate the chemical and surface structure of the Au/CNT. An appropriate CeO_2 content tuned the sizes and chemical states of Au by electron delivery with better metal dispersion. Small CeO_2 crystals that were preferentially neighboring the Au particles facilitated the generation of Au–CeO_2 interfaces, and benefited the continuous supplementation of oxygen species. The collaborative functions between the size effect and surface chemistry accounted for the higher benzaldehyde yield and sustainably stepped-up reaction rates by Au-Ce_5/CNT with 5 wt% CeO_2.

Received 18th October 2021
Accepted 13th December 2021

DOI: 10.1039/d1ra07686h

rsc.li/rsc-advances

Introduction

Benzaldehyde (BzH), as an important intermediate and raw material, is widely applied in medicine, dyestuff, agriculture and chemical industry.[1,2] The traditional processes to produce BzH *via* chlorination of toluene and hydrolysis process are complex with large amounts of toxic wastes, resulting in serious environmental pollution and expensive separation process.[3] In recent years, attention has been paid to the aerobic oxidation of benzyl alcohol (BnOH) in the presence of molecular oxygen or air, mostly using precious and transition metal-based catalysts.[3–5]

Supported Au nanoparticles (Au NPs) with outstanding surface chemistry were preferentially focused due to their excellent selectivity for heterogeneous oxidations compared with other precious metals.[6,7] However, the conversion and stability of gold catalysts during aqueous reaction still need efficient promotions. In fact, one of the accepted strategies will be optimizing the sizes and distribution of Au NPs to maximally obtain coordination-unsaturated Au sites,[8,9] only if the reaction is structure–sensitive with a clear size effect. Although such topic aroused more and more research interest, the main discussion on the surface- and structure-effect of gold catalysts is still in dispute for the aerobic oxidation of BnOH. Zhu *et al.*[10] have encapsulated small Au NPs (5 nm) in the zirconium-based metal organic framework (UIO-66), and the hydrophilic surface of UIO-666 with a high dispersion of Au particles was suggested to be responsible for the good stability and reusability. Haider *et al.*[11] used Au/TiO_2 and Au/CeO_2 as models, and the Au catalyst with average size of 6.9 nm displayed superior activity compared with other samples (1.3–11.3 nm). However, the intrinsic activity that could be revealed by turnover frequency (TOF) was not clearly compared, and the intrinsic influences of the sizes and structure were still unknown. Xu *et al.*[12] studied the influences of the sizes and types of Au clusters in Au_n/LDH (n = 25, 38, ~127) for aerobic BnOH oxidation. Although the Au_{38}/LDH displayed higher TOF value, the TOFs of Au clusters with different sizes were very close in the range of 1464–1605 h^{-1}. On the other hand, Olmos *et al.*[13] claimed that the order of magnitudes of TOF could be significantly influenced by the thermal treatment, support, and especially the type of active sites. The TOFs of different Au–Pd/CeO_2–ZrO_2 samples increased to about 18-fold as the particle sizes grew from 1.7 to 2.0 nm, even if their metal dispersions were identical (1.6 wt%). Hong *et al.*[6] investigated the Au–Pd bimetallic catalysts for the selective oxidation of BnOH. However, the BzH yields of Au–Pd catalysts proved to be irrelevant with the bimetallic particle sizes. Larger Au–Pd particles (15.9 nm) were also able to efficiently convert the BnOH molecules. The reported literature affirmed the essential responsibility of the constructed bimetallic Au–M(O)$_x$ interface (M could be Pd, Pt, Ag, Cu, Ce, Fe, Mg, *etc.*) for the high-efficiency gold catalysts.[14–16] However, the precise understanding of the size- and structure-effect for BnOH oxidation based on bimetallic Au–M(O)$_x$ sites turned out to be an extremely complicate task due to the mingling of hybrid sites. In a word, a controversial discussion exists either

Laboratory of Advanced Materials & Catalytic Engineering (AMCE), School of Chemical Engineering, Dalian University of Technology, Panjin 124221, China. E-mail: changhai@dlut.edu.cn; Fax: +86-411-84986353; Tel: +86-411-84986353

† Electronic supplementary information (ESI) available. See DOI: 10.1039/d1ra07686h

‡ The authors contributed equally to the work.

due to the interferences by the strong interaction between the Au-secondary metal/support, or the multiple parameters induced by the complex system. The understanding of efficient catalysts for aerobic BnOH oxidation should be carried out preliminarily on the monometallic Au catalysts, and the catalytic system affected by a well-constructed interface can thus be boldly explored.

In order to avoid other influencing factors caused by the pre-treatment, strong metal support interaction (SMSI), or depositing process, the support should be properly chosen with the available synthesis strategy.[17–19] Nano carbon materials, *e.g.*, carbon nanotubes (CNT), carbon spheres (CS), carbon fibers (CF) and graphene, are becoming the most popular alternative supports due to their abundant earth-reserves and easily controlled surface chemistry.[20,21] Most important of all, strong synergy is hardly formed between gold and carbon (*e.g.*, CNT) unless special treatment was processed.[22] The weak interaction between gold and CNT acts as a double-edged parameter. It indeed results in the inferior activity, but availably eliminates the interference of SMSI effect during research work. Herein, in this work, monometallic Au catalysts were preliminarily used as the simple model to understand the size and structure effect on the performances of BnOH oxidation. Colloid immobilization method by different coupling agents was applied to obtain gold with controllable size distributions. The structure–sensitivity and the structure–performance relationship were firstly unraveled by the combination of both turnover frequency (TOF) and apparent reaction rate based on monometallic gold samples. Considering the insufficient stability of the monometallic gold catalyst, the CeO_2 dopant was subsequently doped in the catalysts to remedy the oxygen store/releasing ability and distribution of active sites by controlling the metal contents. The construction of the Au–CeO_2 interface, as well as their influences and contribution to the catalytic behavior of aerobic oxidation, were analyzed and correlated.

Results and discussion

Chemical and surface information of Au/CNT

A series of gold colloids have been synthesized according to our previous work[22] and anchored on the surface of purified CNT. The freshly prepared Au-A colloid using PVA as a stabilizer is wine-red, and small particles of 2–3 nm are observed by TEM (Fig. 1(a1)). After metal deposition and calcination, the tubular structure of CNT is well-maintained in different catalysts. The gold nanoparticles (Au NPs) are highly dispersed in Au/CNT-A with an average particle size of 4.9 nm.

The TEM images of the Au/CNT-T_H and Au/CNT-T_L samples using tannic acid as a stabilizer are shown in Fig. 1(b1–b3) and (c1–c3). The average sizes of the Au NPs in the Au/CNT-T_H and Au/CNT-T_L samples are 9.1 and 14.4 nm, respectively, which are larger compared with those in Au/CNT-A. Particles in Au/CNT-Na are even larger and randomly dispersed (Fig. 1(d1–d3)). The statistical result suggests that the average size of Au/CNT-Na is 21.9 nm in Au/CNT-Na based on more than 200 particles.

The crystal structure of different gold catalysts was further detected by the XRD patterns (Fig. 2a). The amorphous carbon was confirmed by the broad and intensive peak at 26.6° (PDF#41-1487), corresponding to the (002) crystal plane of graphite. Several

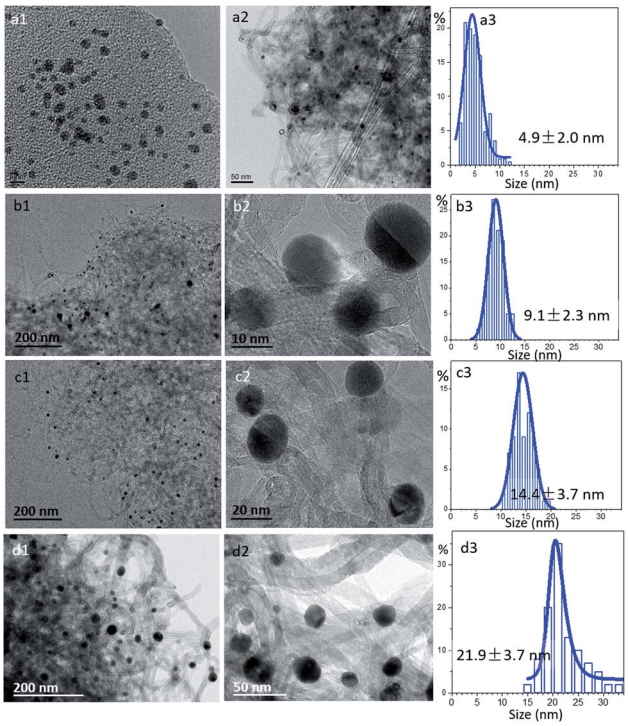

Fig. 1 TEM images and the size distributions of: (a1) TEM images of fresh gold colloid, (a2–a3) Au/CNT-A, (b1–b3) Au/CNT-T_H, (c1–c3) Au/CNT-T_L and (d1–d3) Au/CNT-Na.

diffraction peaks at 38.2°, 44.4°, 64.6° and 77.6° correspond to the (111), (200), (220) and (311) crystal planes of gold (PDF#4-784),[23] suggesting the presence of Au NPs in all samples. The average sizes of Au NPs are calculated to be 5.8 nm, 9.4 nm, and 16.2 nm and 17.3 nm for the Au/CNT-A, Au/CNT-T_H, Au/CNT-T_L, and Au/CNT-Na samples based on the Au(111) face. The XRD results are generally consistent with the statistical results of TEM.

The direct consequences of metal deposition and thermal treatment on the carbon materials are the co-generation of surface defects. Herein, Raman spectra of different samples are displayed in Fig. 2b. Two intensive peaks are observed in the range of 1700–1100 cm^{-1}. The peak at 1343 cm^{-1} labeled as *D* is attributed to the structural defects and the partially disordered structure of the sp^2 carbon. The Raman peak at 1573 cm^{-1} is assigned to the *G* band, which is related with the degree of graphitization.[24] The I_D/I_G value calculated based on the deconvolution of Raman spectra directly reflects the formation degree of the surface defects. The I_D/I_G value of the purified CNT is only 0.94. The deposition of Au NPs caused the higher I_D/I_G value in the range of 1.40–1.57. The variation of the I_D/I_G value changes, along with the average particle sizes by TEM results, is displayed in Fig. 2c. The much higher value of I_D/I_G in the Au/CNT-A and Au/CNT-T_H samples indicates the easier generation of abundant surface defects on carbon after the loading of smaller gold particles.

In fact, compared with the freshly dried samples at 60 °C, the series of Au/CNT samples lost about 5–8% weight mass after calcination, mostly attributed to the surface adsorbed moisture. The surface evolution and generation of defects simultaneously

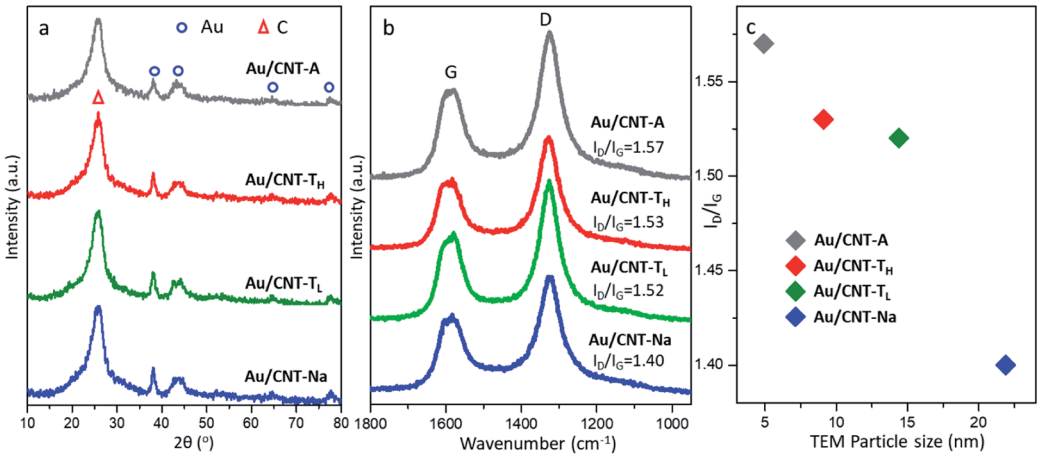

Fig. 2 (a) XRD patterns, (b) Raman spectra and (c) the I_D/I_G value changes along with the particle sizes of different Au/CNT catalysts.

occurred during the thermal treatment,[25,26] with the CNT structure being well-maintained, as shown by the TEM images.

In the XPS spectra of the Au 4f core level (Fig. S1†), typical Au^0 species with binding energy of 84.2 eV and 87.7 eV are observed in all of the catalysts, and belong to the Au $4f_{5/2}$ and $4f_{7/2}$ regions.[27,28] The surface weight ratio of Au/C based on XPS data in Au/CNT-Na is only 2.7 wt% and is much lower than the other gold samples (3.5–4.2 wt%). Considering XPS as a technique detecting the upper layer surface of 5–10 nm, most of the Au signals inside the big Au NPs are beyond the detection limit of the XPS, causing the much lower ratio of Au/C in the Au/CNT-Na sample.

Catalytic evaluation of the Au/CNT catalyst

The results of different Au/CNT samples for the aerobic oxidation of benzyl alcohol (BnOH) under O_2 at ordinary pressure are shown in Fig. 3a. Purified CNT did not offer any BnOH conversion at 80 °C. The Au/CNT-A exhibits 70% selectivity of benzaldehyde (BzH) with 81% conversion of BnOH. The Au/CNT-T_H and Au/CNT-T_L exhibit lower BnOH conversion (77% and 45%, respectively) under the same reaction condition. The BzH selectivity by Au/CNT-T_L is 83.7% and slightly higher than the other samples. The Au/CNT-Na sample displays inferior activity with only 29% BnOH conversion and 67% BzH selectivity. Combining the previous characterization results, it is very interesting that the transformation ability of BnOH by gold catalysts seems to be influenced by their particle sizes. Au/CNT-A and Au/CNT-T_H with smaller particles (4.9 nm & 9.1 nm by TEM) exhibited better conversion of BnOH than the Au/CNT-T_L and Au/CNT-Na samples.

The reaction performance of the typical Au/CNT-A at different temperatures was also detected to understand the influences of the reaction temperature (Fig. 3b). It is suggested that only 48% BnOH is transformed at 40 °C. The rising reaction temperature leads to the increasing BnOH conversion to about 80% at 70–80 °C. However, the BzH selectivity decreases from 83% at 40 °C to 70% at 80 °C due to the facile production of benzaldehyde (BzH) by excessive oxidation. The apparent reaction rates by different Au/CNT samples are calculated (Fig. 3b) at lower temperature (40 °C) to limit the BnOH conversion as less than 20%, and other reaction conditions are listed in Table S1.†

The reaction rate changes in the range of 5–15 mmol g_{Au}^{-1} h^{-1} by different gold catalysts. The apparent reaction rate and catalytic conversion of BnOH by Au/CNT-A and Au/CNT-T_H with smaller particles are indeed superior to the other samples. As the particle sizes become larger, the apparent reaction rates by the Au/CNT-T_L and Au/CNT-Na samples are sharply reduced to 8.4 and 5.3 mmol g_{Au}^{-1} h^{-1}, respectively. The turnover frequency (TOF) based on per Au atom per hour in different catalysts were also calculated (Fig. 3c & Table S1†). The TOFs in the range of 5.83–1.63 × 10^2 h^{-1} oppositely change with the growth of the Au particles. The TOF by Au/CNT-A (4.9 nm by TEM) is about 3.6-fold of that for Au/CNT-Na (21.9 nm). Thus, the particle sizes greatly influence the number of converted BnOH molecules by a single Au atom, suggesting a typical size-sensitive reaction using gold catalysts. Under such circumstance, it can be imagined that the distinctive catalytic behaviors should be mainly induced by the available exposure of active gold sites. Smaller particles have larger surface area and higher percentage of exposed unsaturated Au atoms (surface distribution degree in Table S1†), which are essential for the transformation of BnOH to BzH.

The Au/CNT-A with better catalytic behavior was tested by the circular reaction (Fig. 4a). However, the Au/CNT-A sample gradually encountered deactivation during the circular tests. The conversion of BnOH greatly decreased from 44% to 23% after the 4th reaction cycle. It was previously suggested that a strong interaction between Au and the carbon support was difficult to form unless a supplementary surface property or other chemical element existed.[29] To improve the reactivity and stability under mild conditions, ceria was added as a doping element considering the famous oxygen redox property engaged by CeO_2 and the easily formed contact between gold and reducible metal oxide. Au/CeO_2 (1.5 wt%) and CeO_2/CNT as references were first prepared for the blank tests.

The BnOH conversion by Au/CeO_2 at 80 °C was 40.0% with 84% BzH selectivity, which is inferior to the series of Au/CNT samples. CeO_2/CNT displayed poor activity with less than 10% conversion of BnOH under the same condition. Surprisingly, the reactions by typical Au-Ce_x/CNT samples can be efficiently

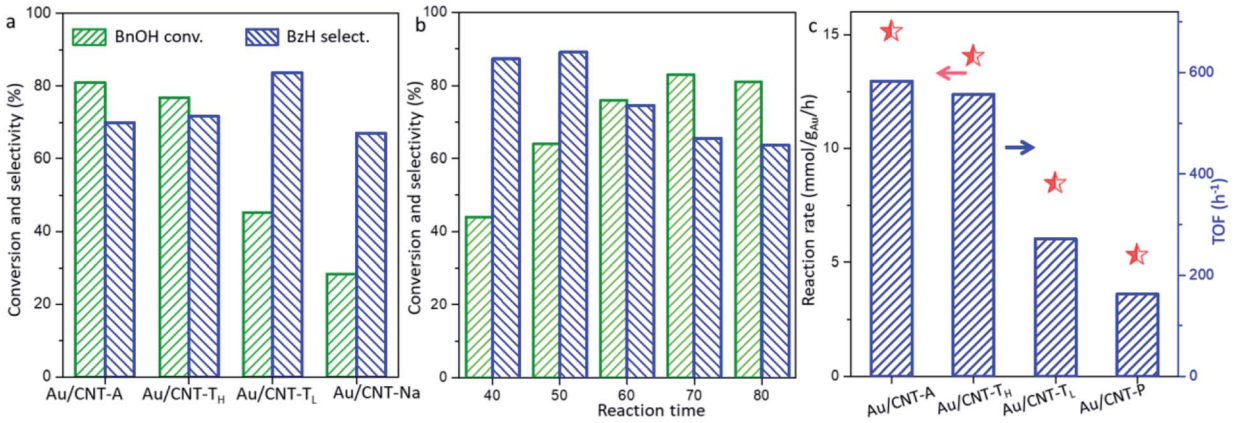

Fig. 3 (a) Catalytic performances of different Au/CNT samples at 80 °C. (b) Catalytic performances of Au/CNT-A *versus* the reaction temperature. (c) Reaction rate and TOF value of the Au/CNT samples for the aerobic oxidation of benzyl alcohol (BnOH) by different catalysts. Reaction conditions: O_2 at ordinary pressure for 3 h, 10 mg catalyst, molar ratio of BnOH/solvent = 1 : 100, if not specified.

catalyzed under even milder conditions at 40 °C. As shown in Fig. 4b, the catalytic performances parabolically change with the ceria contents. As the CeO_2 contents increase from 0 to 5.0%, the conversion of BnOH significantly increases. It reaches 79% BnOH conversion with 85% BzH selectivity by Au-Ce_5/CNT under 40 °C. A further increase of the CeO_2 content causes the obvious decrease of both BnOH conversion and BzH selectivity by the Au-$Ce_{7.5}$/CNT and Au-Ce_{10}/CNT samples. In order to understand the influence of ceria on the stability of the Au-Ce_5/CNT catalyst, the circular reaction was carried out, as shown in Fig. 4c. The catalyst was generally stable during the five-reaction cycles. Only a slight decrease of the BnOH conversion from 79% to 76% was observed with the selectivity of BzH increasing from 85% to 88%. The decoration of ceria greatly enhanced both the catalytic activity and the stability of Au-Ce_5/CNT during the repetition test.

Structure and morphology of Au-Ce_x/CNT

In order to investigate the variation of the crystal structure after CeO_2 doping in the catalyst, the XRD patterns are displayed in Fig. 5a. The diffraction peaks of cubic fluorite CeO_2 are generally locate at 2θ of 28.5°, 33.1°, 47.3° and 56.2° (PDF#34-0394), related to the (111), (200), (220) and (311) crystal planes of ceria.[30] In the Au-Ce_x/CNT samples with lower CeO_2 contents (<5 wt%), CeO_2 is absent possibly due to their high dispersion or small crystal sizes. Formation of clear CeO_2 crystallinity appears in the Au-$Ce_{7.5}$/CNT and Au-Ce_{10}/CNT samples. The average sizes of the Au NPs calculated based on Au(111) are 5.9, 5.0, 9.1, and 10.2 nm, as the CeO_2 contents incrementally increase from 2.5 wt% to 10 wt%. The additional CeO_2 composition changes the crystal sizes of Au. The appropriate content of ceria promotes the formation of smaller Au crystals, while the growth of the Au NPs is induced at higher CeO_2 contents. It was previously reported that CeO_2 was able to enhance the oxygen redox capacity of the catalyst due to its good oxygen storage/release capacity.[31] For better demonstration of such assumption, the H_2-TPR profiles are displayed in Fig. 5b.

The purified CNT displays a small asymmetric reduction peak centered at about 600 °C, which should be attributed to carbon methanation in the presence of H_2.[26] The deposition of

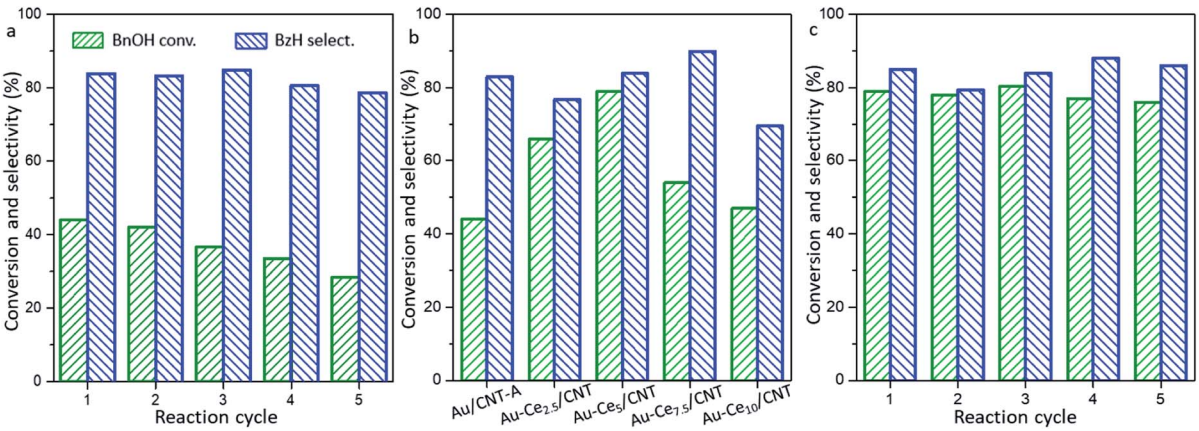

Fig. 4 (a) Stability test of Au/CNT-A, (b) the catalytic performances by different catalysts, and (c) the stability of Au-Ce_5/CNT. Reaction conditions: 40 °C, O_2 at ordinary pressure for 3 h, 10 mg catalyst, molar ratio of BnOH/solvent = 1 : 100.

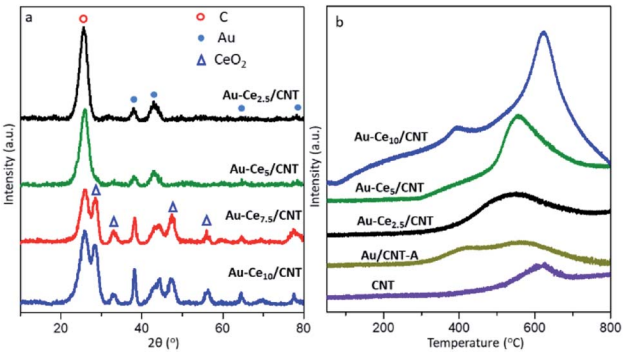

Fig. 5 XRD patterns (a) & H_2-temperature programmed reduction curves (b) of the catalysts with different CeO_2 contents.

Au NPs facilitates the methanation of CNT as the reduction peak area further increases in Au/CNT-A. The reduction of the gold species should be located at a lower position (50–150 °C), which is absent in the detected sample, suggesting that most of the Au species on the surface have been reduced. After CeO_2 doping, the peak area sharply rises with higher CeO_2 contents. Additional reduction peaks in the range of 250–500 °C appear in accordance with the reported reduction peaks of the CeO_2 nanoparticles at 300–600 °C.[32] As the CeO_2 content rises, the peak maximum shifts to higher temperature, especially in the Au-$Ce_{7.5}$/CNT and Au-Ce_{10}/CNT samples. Combining the XRD patterns of different samples, the higher reduction temperature should be caused by the large crystal sizes of CeO_2. Regardless, the CeO_2 doping results in a more intense peak area, indicating the enhancement of the reducibility and redox capacity of the gold catalysts. It is further correlated with the ability to activate/supply active oxygen and lays great importance on the catalytic performances for oxidation. By comparing the H_2 consumption of Au-Ce_x/CNT with Au/CNT-A, the peak area obviously exceeds the stoichiometric value needed for the reduction of CeO_2. It is indicated that the anchored CeO_2 also enhances the methanation of CNT at higher temperature. Interaction should occur between the dispersed CeO_2 crystals and CNT support.

To obtain more surface information on the CNT structure, the XPS spectra in the O 1s region were obtained and are illustrated in Fig. 6. The O 1s spectra is deconvoluted into three overlapped peaks located at 531.4, 532.4, and 533.8 eV, corresponding to the C=O, O–C=O and C–O groups, respectively.[33] Compared to the oxygen content of CNT (O/C atomic ratio of 1.8%, Table S2†), the O/C ratio in Au/CNT-A is 2.3 at%. After ceria decoration, an additional peak around 529.8 eV remarkably appeares in the Au-Ce_x/CNT samples. It should be ascribed to the lattice oxygen.[34,35]

As the ceria contents increase, the total O/C ratios increase from 2.3% in Au/CNT-A to 4.9–7.6% in the Au-Ce_x/CNT samples. The percentages of the lattice oxygen account for 1.3–2.9% in the gold catalysts with different CeO_2 contents. The results of the O 1s spectra are in accordance with the H_2-TPR results, showing that the oxygen supply ability is obviously promoted due to the existence of ceria and supplementation of lattice oxygen.

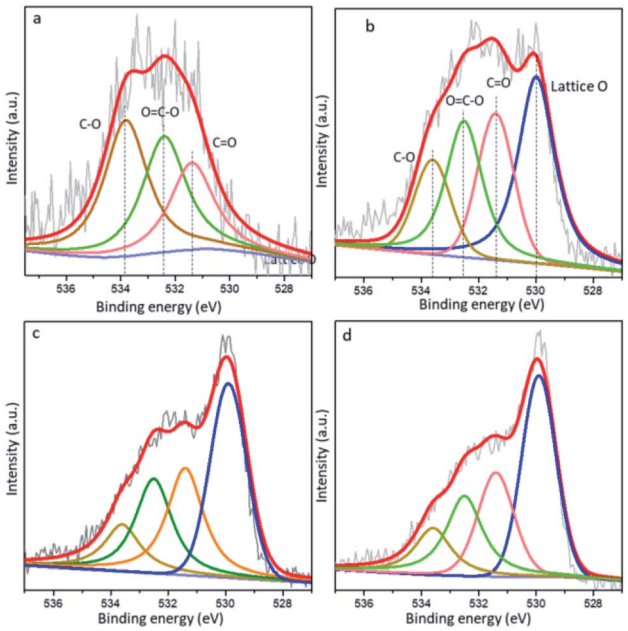

Fig. 6 XPS spectra of the O 1s core level by the (a) Au/CNT, (b) Au-$Ce_{2.5}$/CNT, (c) Au-Ce_5/CNT and (d) Au-Ce_{10}/CNT samples.

The XPS spectra of the Au 4f core level by Au/CNT-A and Au-Ce_x/CNT are illustrated in Fig. 7. As mentioned above, only metallic Au^0 exists in the monometallic Au/CNT-A. Different from Au/CNT-A, positively charged Au species ($Au^{\delta+}$) are generated and detected in the series of Au-Ce_x/CNT samples, which are 5%, 10% and 9% in the total gold species of the Au-$Ce_{2.5}$/CNT, Au-Ce_5/CNT and Au-Ce_{10}/CNT samples, respectively. $Au^{\delta+}$ was also reported to exist in metal oxide promoted gold catalysts, and was beneficial for heterogeneous reactions.[36] It is inferred that the specific interaction and interfaces have been formed between gold and ceria. In the series of Au-Ce_x/CNT samples, connection between Au and the ceria-decorated CNT likely happenes and electrons are delivered from gold to ceria to give the more positively charged $Au^{\delta+}$ species.

The TEM images of Au-Ce_5/CNT are shown in Fig. 8. Small Au NPs around 3.8 nm are highly dispersed in the catalyst. It is difficult to directly identify the location of CeO_2 due to the poor contrast of the TEM images in low magnification. In this case, high-resolution TEM images were carried out. The Au particles and ceria crystals can be identified by counting the inter-planar distances. Both typical lattice distances of the Au(111) phase and ceria can be frequently observed on the surface. A small amount of isolated ceria is also present, while most of the Au NPs are adjacent to the ceria crystals, either due to the reported selective adsorption/deposition between metal (oxides) or the ubiquitous dispersion of small ceria crystals.[37] The HAADF-STEM elemental-mapping of the Au-Ce_5/CNT also proved that the Ce signals were uniformly dispersed on the surface of CNT (Fig. S2†). It is also interesting to note that mutual interfaces were more frequently built and detected between the Au(111) and CeO_2(400) crystal phases. The construction of the Au–CeO_2

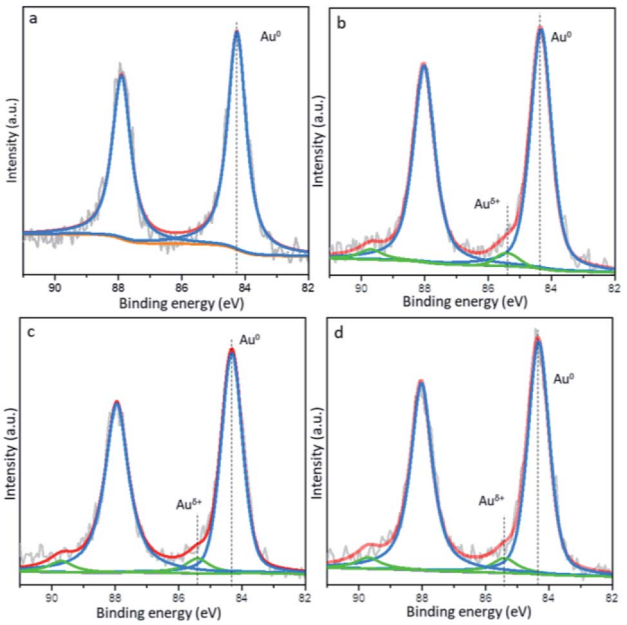

Fig. 7 XPS spectra of the Au 4f core level by the (a) Au/CNT, (b) Au-$Ce_{2.5}$/CNT, (c) Au-Ce_5/CNT and (d) Au-Ce_{10}/CNT samples.

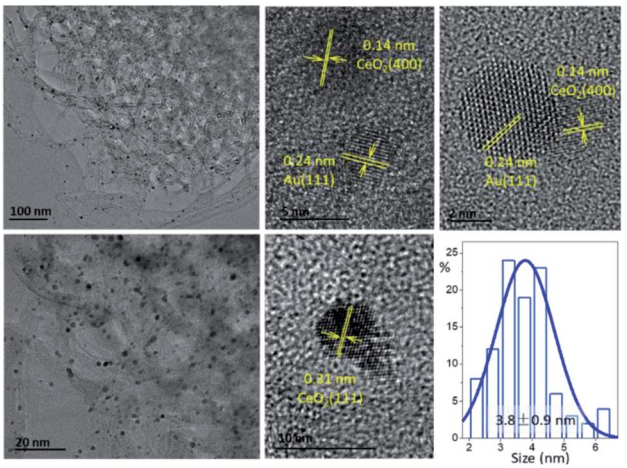

Fig. 8 TEM images and size distribution of the typical Au-Ce_5/CNT sample.

interface facilitates the oxygen supply from the CeO_2 near the Au NPs and accelerates the oxidation rate of BnOH.

The major surface and chemistry factors influencing the catalytic behaviors of Au catalysts are now well-known and can be summarized as follows: (i) the particle sizes of gold, and (ii) the oxygen activation and redox properties enhanced by the additional metal oxide. After ceria decoration, both reaction rates at 40 °C and 50 °C by typical Au-Ce_x/CNT (x = 2.5, 5, 10) samples were calculated. The reaction rates by different Au-Ce_x/CNT samples were in the range of 9.4–15.7 mmol g_{Au}^{-1} h^{-1} at 40 °C, which grew in inverse proportion to the average particle sizes – either by XRD or TEM results – in the Au/CNT and the Au-Ce_x/CNT systems (Fig. 9 & Table S3†). The regular decrease of reaction rates was also observed with the increasing Au sizes. Compared with the reaction rate of Au/CNT-A at 40 °C (7.6 mmol g_{Au}^{-1} h^{-1}), the reaction rates of the Au-Ce_x/CNT system with similar sizes of particles were greatly promoted, which should be a combined effect from multiple parameters beyond the size effect.

In fact, one problem with using monometallic gold catalysts for the selective oxidation of BnOH is that the adsorption/dissociation of both O_2 and BnOH molecules are indispensable on the surface of the monometallic gold catalyst. Herein, the competitive adsorption between BnOH and O_2 during the reaction was frequently reported, following the Langmuir–Hinshelwood model.[38] The sizes of the Au NPs become essential since smaller particles exposes more gold sites to activate/dissociate reactant molecules with higher TOF. H_2-TPR results reflect the much better redox properties of the series of Au-Ce_x/CNT after ceria doping, either due to the supplementation of the CeO_2 lattice oxygen or O_2 dissociatively adsorbed on ceria nearby Au NPs. An even higher CeO_2 content changes the surface chemistry, however, at the cost of forming larger Au NPs and separated ceria crystals. Therefore, the appropriate CeO_2 content is significant for the oxidation of BnOH. A high dispersion of CeO_2 around the Au NPs was confirmed by XRD and TEM in the Au-Ce_5/CNT sample. The close contact between gold and ceria provides new reaction sites at the interfaces, and the active oxygen species during the reaction can be continuously supplied.

Under such circumstance, Au NPs with smaller sizes provide the effective transformation of BnOH with a higher number of available exposed active sites, while the additional ceria promotes the activation/supplementation of the oxygen species during the reaction. The prerequisite for the successful and fast transformation from BnOH to BzH can thus be achieved by the current system.

Based on the above discussion, the available reaction pathway by the ceria-promoted gold catalyst is displayed in

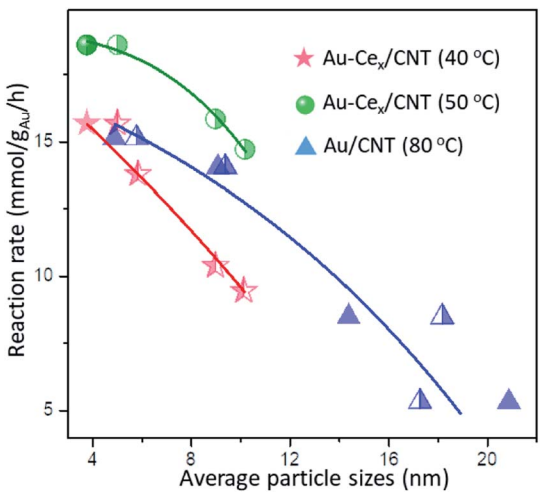

Fig. 9 Reaction rate and TOF value of the Au/CNT samples at 40 °C, and the correlation between the reaction rates and average particle sizes detected using XRD (half-hollow icon) and TEM (solid icon).

Scheme 1. Molecular oxygen was suggested to take part in the reaction by forming a hydroxide or hydroperoxo-species on the surface of the metal oxide (*e.g.*, CeO_2) instead of directly dissociating to oxygen atoms,[39,40] which was suggested to be beneficial for abstracting the β-hydride of the alcohol. H_2O_2 was also reported to be detected during the oxidation of BnOH, especially if there was an active metal (oxide) as the doping element near the Au NPs.[41,42]

During the reaction, the ceria composition near the small Au NPs is responsible for supplying the active oxygen species $^{\bullet}O_2^-$, by either supplementation from the lattice oxygen or adsorption/dissociation of gaseous molecular oxygen. The proton abstraction of molecular BnOH subsequently occurred by forming –OOH on the surface of the neighboring ceria. The deprotonated BnOH* is adsorbed on the surface of gold with positively charged $Au^{\delta+}$ (as detected by XPS spectra) to form an alkoxide intermediate after step I.[43] The β-H in BnOH* is then bonded with gold atoms (step II) and is eliminated to produce the gold-hydride intermediate during step III. BzH is simultaneously released, leaving the proton occupying the surface of Au NPs. The cleavage of C–H was reported to be the rate-determining step for BnOH oxidation,[44] which should be preferentially operated by unsaturated sites. Herein, samples with smaller sizes were related with the better yield of BzH. The initial surface of the ceria-promoted gold catalyst can be finally recovered by releasing the H_2O_2 molecules (step IV). The new circulation was continuously operated until the oxidation process was fulfilled.

Experimental

Materials and synthesis

The as-received carbon nanotubes (CNT) were supplied by Shandong Dazhan Nano Materials Company. Chloroauric acid ($HAuCl_4 \cdot 3H_2O$), sodium borohydride, ceria nitrate, tannic acid, benzyl alcohol and other reactants were purchased from Sinopharm Chemical Reagent Company. Polyvinyl alcohol (PVA, M_w = 30 000–70 000), sodium citrate, and *p*-xylene were provided by Macklin Biochemical Company.

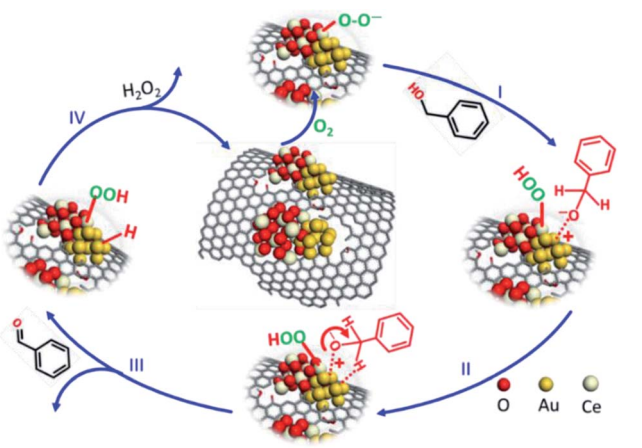

Scheme 1 The available reaction pathway *via* the CeO_2-promoted gold catalyst.

Preparation of different gold colloids

A series of gold colloids were synthesized and used as gold precursors. The Au-A colloid was prepared using polyvinyl alcohol (PVA) as a protector and reduced by $NaBH_4$. The $HAuCl_4 \cdot 4H_2O$ aqueous solution (10^{-3} mol L^{-1}) was mixed with a certain amount of 1% PVA solution in a 250 mL beaker (weight ratio of PVA/Au is 5 : 1). 0.1 mol L^{-1} $NaHB_4$ was then added to reduce the $HAuCl_4$ to gold colloid (molar ratio of $NaBH_4$/Au = 5 : 1). The color of the solution changed to wine-red, indicating the successful preparation of the gold colloid, and was denoted as Au-A. Tannic acid was also used as a stabilizing agent for Au NPs. A certain amount of chloroauric acid aqueous solution was added to a beaker and heated to 65 °C. Sodium borohydride solution (0.1 mol L^{-1}) and tannic acid (0.1 mol L^{-1}) were subsequently added to the above solution under continuous stirring. The solution was further stirred for 10 minutes for complete reduction of Au^{3+}. The resulting gold colloids were labelled as Au-T_H and Au-T_L, with the molar ratios of tannic acid/Au as 5 : 1 and 2 : 1, respectively. The Au–Na colloid was prepared using sodium citrate as a stabilizer and reducer. An appropriate amount of 0.1 mol L^{-1} sodium citrate aqueous solution was added to the $HAuCl_4$ solution at 80 °C until the color turned purple under stirring for 30 min. The weight ratio of sodium citrate/Au was kept at 3.3 : 1.

Preparation of Ce_x/CNT

A mass of 5 g purified CNT was dissolved in 60 mL of deionized water with a certain amount of cerium nitrate. The mixture was placed in a three-neck bottle in an oil bath. After heating to 90 °C, 30 mL sodium hydroxide solution (0.005 g mL^{-1}) was added to the flask and stirred for 5 h, with the pH value kept at 9–10. After the solution was cooled down to room temperature, the catalyst was washed with deionized water until neutral and dried in an oven at 60 °C overnight. The sample was heated to 400 °C and calcined in Ar for 2 h. The supports were denoted as Ce_x/CNT, and x% suggested the weight ratio of CeO_2 to carbon (x = 1.5, 2.5, 5, 7.5, or 10).

Preparation of Au/CNT and Au-Ce_x/CNT

The series of gold catalysts were synthesized by colloidal immobilization method. A mass of 2 g CNT or 2 g Ce_x/CNT was poured into the colloid synthesized in 2.1.1, and aged for 16 hours under continuous stirring. The suspension was then filtered and washed by deionized water several times to remove the residual Cl^-. The black powder was dried in an oven at 60 °C overnight and calcined at 300 °C for 3 h in 25% (v/v) O_2 balanced with Ar. The final catalysts were denoted as Au/CNT-A, Au/CNT-T_H, Au/CNT-T_L, Au/CNT-Na, and Au-Ce_x/CNT (using Au-A colloid, x = 1.5, 2.5, 5, 7.5, 10) for short, according to the detailed colloids and supports.

Characterization

X-ray Diffraction (XRD) was carried out on a Shimadzu 7000S diffractometer with Cu Kα radiation ($\lambda = 1.5418$ Å), with a scanning rate of 3° min^{-1} in the range of 10°–80°. The average crystal sizes were calculated according to the Scherrer formula. The Raman spectra were recorded using a 532 nm laser source by a Renishaw inVia confocal Raman microscope. The value of I_D/I_G was calculated by the corresponding area of the Raman peaks located at 1343 cm^{-1} and 1573 cm^{-1} identified after peak deconvolution. X-ray photoelectron spectroscopy (XPS) was achieved on the ESCALAB™ 250Xi (Thermo Fisher, USA). The charge correction was based on the C 1s peak at 284.6 eV. The X-ray excitation source was Al Kα. Transmission electron microscopy (TEM) was performed on a FEI Tecnai G2 F30 electron microscope at an acceleration voltage of 120 kV. The average sizes of the particles were calculated based on more than 200 particles. H_2-temperature-programmed reduction (H_2-TPR) was carried out on a Quantachrome ChemBET 3000 Chemisorber apparatus with a gas flow rate of 30 mL min^{-1}. The reduction process was carried out by increasing the temperature from 50 °C to 800 °C at a heating rate of 10 °C min^{-1}.

Aerobic oxidation of benzyl alcohol

Benzyl alcohol (BnOH) and 5 g *p*-xylene were added to a 25 mL three-necked flask in the presence of NaOH and the catalyst, and put into an oil bath. Continuous oxygen flow was kept at 40 mL min^{-1} after the temperature was set to the target value. After reaction, the solution was cooled down to room temperature and was analyzed on the gas chromatograph (Agilent GC-7890) after filtration. Then, the conversion of BnOH and the selectivity of benzaldehyde (BzH) were calculated by internal standard method. The conversion of BnOH and the selectivity for BzH can be calculated as follows:

$$[\mathrm{Conv}_{\mathrm{BnOH}}] = \frac{n_0 - n_{\mathrm{BnOH}}}{n_0} \times 100\%$$

$$[\mathrm{Sel}_{\mathrm{BzH}}] = \frac{n_{\mathrm{BzH}}}{n_0 - n_{\mathrm{BnOH}}} \times 100\%$$

where n_0 is the initial mole number of BnOH, and n_{BnOH} and n_{BzH} are the final mole numbers of BnOH and BzH, respectively.

The turnover frequency (TOF) of a typical sample was calculated based on the statistical results of the TEM images by the following equation:

$$\mathrm{TOF}\ \left(\mathrm{h}^{-1}\right) = \frac{N_{\mathrm{BnOH}}}{N_{\mathrm{Au}} \times D_{\mathrm{m}} \times t}$$

The N_{BnOH} denotes the transferred number of BnOH molecules, which was controlled by lowering the reaction temperature (40 °C) and catalyst dosage; t is the reaction time in hour; the N_{Au} is the total number of Au atoms in the catalyst; D_{m} is the surface dispersion degree of Au, and can be calculated by the equation between the particle area (S_{NP}) and weight (m_{NP}) of one Au NP, as well as the sectional area of a Au atom (S_{Au}):

$$D_{\mathrm{m}} = \frac{S_{\mathrm{NP}}/S_{\mathrm{Au}} \times \overline{M}_{\mathrm{Au}}}{m_{\mathrm{NP}} \times N_{\mathrm{A}}}$$

$\bar{M}_{\mathrm{Au}}$ is the molar mass of Au (197 g mol^{-1}) and N_{A} is the Avogadro constant.

Conclusion

In this work, a series of uniform gold colloids with distinctive size distributions were designed by optimizing the coupling agents, and anchored on the surface of CNT by colloid immobilization method. The as-synthesized gold catalysts were used for the aerobic oxidation of benzyl alcohol. The much-improved transformation ability of benzyl alcohol proved to be a direct size-sensitive property of the reaction by gold catalysts. However, the Au/CNT-A sample – with particle sizes of 4.9 nm and better catalytic performances – lacked long-term cycle stability. CeO_2 was herein used as an additional composition for further promotion of the gold catalysts. The chemistry and surface properties of catalysts were greatly modulated according to the ceria contents. CeO_2 doping greatly modified the oxygen redox property and the chemical state of Au NPs. An appropriate CeO_2 content facilitated the formation of Au–CeO_2 interfaces. Even higher ceria contents induced the obvious aggregation of both gold particles and ceria crystals, leading to the reasonable impairment of the gold catalyst. The 5 wt% Au-Ce_5/C sample provided better conversion of benzyl alcohol and a reaction rate of 15.7 mmol g_{Au}^{-1} h^{-1} at 40 °C.

Author contributions

Conceptualization & methodology, C. Liang and J. Luo; validation, F. Shan, Y. Zhou and S. Yang; formal analysis, J. Luo and F. Shan; data curation, F. Shan, Y. Zhou and S. Yang; writing – review and editing, C. Liang and J. Luo; supervision, C. Liang and J. Luo; project administration, C. Liang; funding acquisition, C. Liang and J. Luo. All authors have read and agreed to the published version of the manuscript.

Conflicts of interest

There are no conflicts to declare.

Acknowledgements

This work was supported by the National Natural Science Foundation of China (21978031 & 21802015), Science and Technology Innovation Fund in Dalian City (2021J12GX025) and Liaoning Revitalization Talent Program (XLYC1908033).

Notes and references

1 Z. Zhou, Y. Xie, W. Zhu, H. Zhao, N. Yang and G. Zhao, *Appl. Catal., B*, 2021, **286**, 119868.
2 Y.-X. Tan, Z.-M. Chai, B.-H. Wang, S. Tian, X.-X. Deng, Z.-J. Bai, L. Chen, S. Shen, J.-K. Guo, M.-Q. Cai, C.-T. Au and S.-F. Yin, *ACS Catal.*, 2021, **11**, 2492–2503.

3 J. Liu, S. Zou, J. Wu, H. Kobayashi, H. Zhao and J. Fan, *Chin. J. Catal.*, 2018, **39**, 1081–1089.
4 J. Xu, J.-K. Shang, Y. Wang, Y. Chen and Y.-X. Li, *Catal. Lett.*, 2016, **147**, 328–334.
5 K. F. Zhang, Y. X. Liu, J. G. Deng, L. Jing, W. B. Pei, Z. Han, X. Zhang and H. X. Dai, *ChemCatChem*, 2019, **11**, 6398–6407.
6 Y. L. Hong, X. L. Jing, J. L. Huang, D. H. Sun, T. Odoom-Wubah, F. Yang, M. M. Du and Q. B. Li, *ACS Sustainable Chem. Eng.*, 2014, **2**, 1752–1759.
7 H. She, H. Zhou, L. Li, L. Wang, J. Huang and Q. Wang, *ACS Sustainable Chem. Eng.*, 2018, **6**, 11939–11948.
8 A. Holm, E. D. Goodman, J. H. Stenlid, A. Aitbekova, R. Zelaya, B. T. Diroll, A. C. Johnston-Peck, K.-C. Kao, C. W. Frank, L. G. M. Pettersson and M. Cargnello, *J. Am. Chem. Soc.*, 2020, **142**, 14481–14494.
9 Y. Pan, G. Wu, Y. He, J. Feng and D. Li, *J. Catal.*, 2019, **369**, 222–232.
10 J. Zhu, P. C. Wang and M. Lu, *Appl. Catal., A*, 2014, **477**, 125–131.
11 P. Haider, B. Kimmerle, F. Krumeich, W. Kleist, J. D. Grunwaldt and A. Baiker, *Catal. Lett.*, 2008, **125**, 169–176.
12 Y. Xu, J. Li, J. Zhou, Y. Liu, Z. Wei and H. Zhang, *J. Catal.*, 2020, **389**, 409–420.
13 C. M. Olmos, L. E. Chinchilla, A. Villa, J. J. Delgado, A. B. Hungría, G. Blanco, L. Prati, J. J. Calvino and X. Chen, *J. Catal.*, 2019, **375**, 44–55.
14 P. Wu, Z. He, Y. Liu, L. Song, C. Wang, E. Muhumuza, P. Bai, L. Zhao, S. Mintova and Z. Yan, *ACS Appl. Mater. Interfaces*, 2021, **13**, 49780–49792.
15 S. Dai, T.-H. Huang, W.-I. Liu, C.-W. Hsu, S.-W. Lee, T.-Y. Chen, Y.-C. Wang, J.-H. Wang and K.-W. Wang, *Nano Lett.*, 2021, **21**, 9293–9300.
16 Y. Li, S. Li, A. V. Nagarajan, Z. Liu, S. Nevins, Y. Song, G. Mpourmpakis and R. Jin, *J. Am. Chem. Soc.*, 2021, **143**, 11102–11108.
17 J. J. Luo, Y. N. Dong, C. Petit and C. H. Liang, *Chin. J. Catal.*, 2021, **42**, 670–693.
18 T. Ishida, T. Murayama, A. Taketoshi and M. Haruta, *Chem. Rev.*, 2020, **120**, 464–525.
19 M. Sankar, Q. He, R. V. Engel, M. A. Sainna, A. J. Logsdail, A. Roldan, D. J. Willock, N. Agarwal, C. J. Kiely and G. J. Hutchings, *Chem. Rev.*, 2020, **120**, 3890–3938.
20 R. H. Adnan and V. B. Golovko, *Catal. Lett.*, 2018, **149**, 449–455.
21 P. Hao, M. Zhang, W. Zhang, Z. Tang, N. Luo, R. Tan and D. Yin, *Catal. Sci. Technol.*, 2018, **8**, 4463–4473.
22 M. H. Xu, S. Y. Jiang, B. Jiang and J. B. Zheng, *Int. J. Environ. Anal. Chem.*, 2019, **99**, 913–927.
23 L. Liu, X. Zhou, Y. Yan, J. Zhou, W. Zhang and X. Tai, *Polymers*, 2018, **10**, 1089.
24 H. T. Kim, H. Shin, I. Y. Jeon, M. Yousaf, J. Baik, H. W. Cheong, N. Park, J. B. Baek and T. H. Kwon, *Adv. Mater.*, 2017, **29**, 1702747.
25 J. J. Luo, Y. F. Liu, H. Wei, B. L. Wang, K. H. Wu, B. S. Zhang and D. S. Su, *Green Chem.*, 2017, **19**, 1052–1062.
26 J. J. Luo, E. H. Qu, Y. X. Zhou, Y. N. Dong and C. H. Liang, *Appl. Catal., A*, 2020, **602**, 117669.
27 L. Liu, X. Tai, X. Zhou, J. Hou and Z. Zhang, *J. Alloys Compd.*, 2019, **790**, 326–336.
28 J. J. Luo, Y. F. Liu, Y. M. Niu, Q. Jiang, R. Huang, B. S. Zhang and D. S. Su, *Nanoscale*, 2017, **9**, 15033–15043.
29 J. Luo, H. Wei, Y. Liu, D. Zhang, B. Zhang, W. Chu, C. Pham-Huu and D. S. Su, *Chem. Commun.*, 2017, **53**, 12750–12753.
30 X. Zhang, L. Dai, Y. Liu, J. Deng, L. Jing, X. Yu, Z. Han, K. Zhang and H. Dai, *Catal. Sci. Technol.*, 2020, **10**, 3755–3770.
31 P. X. Huang, F. Wu, B. L. Zhu, X. P. Gao, H. Y. Zhu, T. Y. Yan, W. P. Huang, S. H. Wu and D. Y. Song, *J. Phys. Chem. B*, 2005, **109**, 19169–19174.
32 Y. Zhang, L. Liang, Z. Chen, J. Wen, W. Zhong, S. Zou, M. Fu, L. Chen and D. Ye, *Appl. Surf. Sci.*, 2020, **516**, 146035.
33 R. Ramesh, A. Nair, A. Jayavel, K. Sathiasivan, M. Rajesh, S. Ramaswamy and K. Tamilarasan, *Chem. Pap.*, 2020, **74**, 4533–4545.
34 Y. Dong, J. Luo, S. Li and C. Liang, *Catal. Commun.*, 2020, **133**, 105843.
35 M. Lykaki, E. Pachatouridou, S. A. C. Carabineiro, E. Iliopoulou, C. Andriopoulou, N. Kallithrakas-Kontos, S. Boghosian and M. Konsolakis, *Appl. Catal., B*, 2018, **230**, 18–28.
36 J. J. Luo, Y. F. Liu, L. Y. Zhang, Y. J. Ren, S. Miao, B. S. Zhang, D. S. Su and C. H. Liang, *ACS Appl. Mater. Interfaces*, 2019, **11**, 35468–35478.
37 J. Zecevic, G. Vanbutsele, K. P. de Jong and J. A. Martens, *Nature*, 2015, **528**, 245–248.
38 W. Z. Yi, W. T. Yuan, Y. Meng, S. H. Zou, Y. H. Zhou, W. Hong, J. W. Che, M. J. Hao, B. Ye, L. P. Xiao, Y. Wang, H. Kobayash and J. Fan, *ACS Appl. Mater. Interfaces*, 2017, **9**, 31853–31860.
39 Z. X. Yan, Z. H. Xu, L. Yue, L. Shi and L. Y. Huang, *Chin. J. Catal.*, 2018, **39**, 1919–1928, DOI: 10.1016/S1872-2067(18)63143-2.
40 T. T. Jiang, C. C. Jia, L. C. Zhang, S. R. He, Y. H. Sang, H. D. Li, Y. Q. Li, X. H. Xu and H. Liu, *Nanoscale*, 2015, **7**, 209–217.
41 I. F. Teixeira, M. S. Homsi, R. S. Geonmonond, G. F. S. R. Rocha, Y. K. Peng, I. F. Silva, J. Quiroz and P. H. C. Camargo, *Nanomaterials*, 2020, **10**, 1530.
42 P. Christopher, H. L. Xin and S. Linic, *Nat. Chem.*, 2011, **3**, 467–472.
43 D. Tsukamoto, Y. Shiraishi, Y. Sugano, S. Ichikawa, S. Tanaka and T. Hirai, *J. Am. Chem. Soc.*, 2012, **134**, 6309–6315.
44 A. Abad, A. Corma and H. Garcia, *Chem.–Eur. J.*, 2008, **14**, 212–222.